Am J Transl Res 2026;18(10):9251-9269
www.ajtr.org /ISSN:1943-8141/AJTR0176093

Original Article

RAD51 inhibition ameliorates secondary hyperparathyroidism: bioinformatic prediction and experimental verification

Xuemei Sun[1*], Qingqing Luo[2*], Shen Yan[2], Fuli Yang[2], Jiajun Zhou[2], Fanze Yang[2], Yijing Cheng[3], Wandong Yang[2], Yongfeng Li[2]

[1]Department of Cardiology, The First People's Hospital of Kunming, Kunming, Yunnan, China; [2]Department of Ultrasound, The First People's Hospital of Kunming, Kunming, Yunnan, China; [3]Department of Ultrasound, The Third People's Hospital of Kunming, Kunming, Yunnan, China. [*]Equal contributors.

Received August 17, 2026; Accepted September 30, 2026; Epub October 15, 2026; Published October 30, 2026

Abstract: Secondary hyperparathyroidism (SHPT) is a frequent complication of chronic kidney disease (CKD), and the transition of parathyroid hyperplasia from diffuse to nodular marks the shift from a pharmacologically manageable to a treatment-refractory state, yet the molecular basis of this transition remains unclear. We analyzed the GSE75886 dataset to compare differentially expressed genes from 8 nodular hyperplasia (NHD) and 5 diffuse hyperplasia (DHD) samples in SHPT. Key genes were screened by a combination of functional enrichment (GO/KEGG), protein-protein interaction network analysis, and ROC curve assessment. Meanwhile, a 5/6 nephrectomy (5/6 Nx) combined with a high-phosphorus diet rat model was established for in vivo validation experiments. While being fed a high-phosphorus diet, SHPT model rats received intraperitoneal injections of IBR2 (2 or 10 mg/kg) three times per week for four consecutive weeks; the cinacalcet group received cinacalcet (10 mg/kg) by oral gavage on the same schedule (three times per week for four weeks). After the treatment, parathyroid histomorphology, the Ki-67 positivity rate, serum biochemical parameters and the protein expression of RAD51, γH2AX, and cleaved caspase-3 were assessed. We identified 914 differentially expressed genes in our analysis. GO and KEGG enrichment linked these genes to DNA replication regulation, ferroptosis, and non-homologous end-joining. Protein-protein interaction network and topology analyses pinpointed eight hub genes (*CTNNB1, ALB, BCL2, H3C13, H4C6, RAD51, IL10*, and *SOX2*), with RAD51 achieving perfect discriminatory performance (AUC = 1.000). Among these, *Rad51* was the most highly upregulated (5.87-fold) in the rat SHPT model and was therefore pursued for functional validation. Blocking RAD51 pharmacologically attenuated parathyroid hyperplasia (reducing Ki-67 from 20.62% to 3.03%), lowered circulating PTH, and reestablished normocalcemia. By contrast, cinacalcet lowered PTH but failed to normalize calcium concentrations. At the mechanistic level, RAD51 preserves DNA repair integrity (γH2AX accumulation signifies repair dysfunction) and constrains apoptosis; its inhibition unleashes cleaved-caspase-3-driven cell death, distinguishing it from cinacalcet's mode of action. *RAD51* inhibition alleviates SHPT through impaired DNA repair and enhanced parathyroid cell apoptosis. These findings identify RAD51 as a novel therapeutic target for SHPT, with potential relevance to nodular hyperplasia.

Keywords: Secondary hyperparathyroidism, RAD51, 5/6 nephrectomy, diffuse hyperplasia, nodular hyperplasia, cinacalcet

Introduction

Secondary hyperparathyroidism (SHPT) represents a major disorder frequently associated with chronic kidney disease (CKD), with a prevalence of up to 49.5% among CKD patients worldwide [1, 2]. Its pathogenesis is closely associated with mineral metabolism disorders, including hypocalcemia, hyperphosphatemia, and decreased concentrations of the vitamin D hormone (1,25-dihydroxyvitamin D_3) [3, 4]. In the early stages of the disease, diffuse hyperplasia of principal cells in the parathyroid glands leads to markedly elevated production and release of PTH [5-7]. CKD can lead to secondary parathyroid hyperplasia and adenoma formation, which are associated with increased serum PTH levels and further cause systemic

multi-organ damage, significantly impairing patients' quality of life [8]. Notably, prolonged hemodialysis duration significantly elevates the risk of calcium-phosphate metabolic disturbances and SHPT, while the proportion of patients requiring parathyroidectomy also increases [9, 10]. The transition from diffuse to nodular parathyroid hyperplasia marks a pivotal pathological milestone in SHPT progression and serves as a primary driver of drug-refractory and postoperative relapse [11, 12]. It is widely recognized that nodular parathyroid hyperplasia is characterized by reduced VDR/CaSR expression, increased proliferative activity, and refractoriness to pharmacological agents, such that medical management alone is no longer sufficient to halt its progression [13, 14]. Therefore, identifying biomarkers that can slow the transition of parathyroid hyperplasia undergoing nodular transformation is critical for improving patient outcomes.

Shen et al. validated the GSE75886 dataset using machine learning, identifying five SHPT-associated genes in the progression of parathyroid hyperplasia from diffuse to nodular patterns [15]. Týcová et al. employed alternative bioinformatics algorithms on the same dataset and uncovered an additional panel of core driver genes - *RANGRF*, *EXOC8*, *PIN1*, and *CACYBP* [16]. Together, these findings attest to the robustness of the GSE75886 dataset and illustrate that divergent analytical approaches can capture complementary molecular signatures, implying that this dataset retains considerable untapped potential for novel target discovery through innovative analytical paradigms. RAD51 is the key recombination enzyme that mediates homologous recombination (HR) repair; by mediating the insertion of single-stranded DNA into homologous double-stranded templates and D-loop assembly, it is indispensable for repairing double-strand DNA breaks. Qiu et al. demonstrated that elevated RAD51 markedly upregulated osteogenic markers including Runx2, OCN, and COL1A1. Mechanistically, RAD51 overexpression activated the IGF1 signaling axis, and the IGF1R inhibitor BMS754807 reversed both the pro-osteogenic action and IGF1 pathway activation elicited by oe-RAD51 [17]. Schürmann et al. showed that B02-mediated RAD51 inhibition impairs HR repair, potentiates cytotoxic responses to DNA damage, and triggers mitochondrial dysfunction and caspase-driven apoptosis in colorectal and mammary carcinoma cells [18]. Bright et al. confirmed that targeting RAD51 can modulate the responsiveness of cancer cells to DNA-damaging therapies [19]. However, previous studies on RAD51 have primarily focused on oncology, genetic disorders, and bone metabolism, while its expression patterns, regulatory mechanisms, and pathological significance in SHPT associated with CKD have not been reported.

We therefore interrogated the GSE75886 dataset to identify differentially expressed genes (DEGs) distinguishing diffuse from nodular parathyroid hyperplasia in SHPT, seeking key regulatory molecules. An SHPT rat model was then established via 5/6 nephrectomy and a high-phosphate diet, and candidate genes (*Sox2, Bcl2, H3C13, Ctnnb1, IL10, H4c6, Rad51, and Alb*) were validated by qPCR, Western blot, and IHC at both RNA and protein levels. We further assessed the impact of RAD51 inhibition on renal function, calcium-phosphate balance, chief cell hyperplasia, Ki-67 positive rate, and apoptosis/DNA damage markers (cleaved caspase-3, γH2AX) in SHPT rats. Collectively, this study investigated how RAD51 drives parathyroid hyperplasia, offering novel therapeutic targets and experimental rationale for impeding the diffuse-to-nodular transition.

Materials and methods

Experimental design

This study consisted of two independent animal experiments. In Experiment 1, rats were randomly assigned to two groups (n = 3 per group): Sham (without ligation or excision) and Model (5/6 nephrectomy). The Sham group was maintained on a normal-phosphate diet (0.8% phosphorus), and the Model group was maintained on a high-phosphate diet (1.2% phosphorus) for 4 weeks. In Experiment 2, after left nephrectomy, 5/6 nephrectomy rats were randomly assigned to four groups (n = 3 per group): (i) SHPT model (vehicle control); (ii) SHPT + IBR2 low-dose (2 mg/kg); (iii) SHPT + IBR2 high-dose (10 mg/kg); and (iv) SHPT + cinacalcet positive control (10 mg/kg). IBR2 (TargetMol, T11600) was administered by intraperitoneal injection, and cinacalcet (TargetMol, T8403) was administered by oral gavage, three times per week for

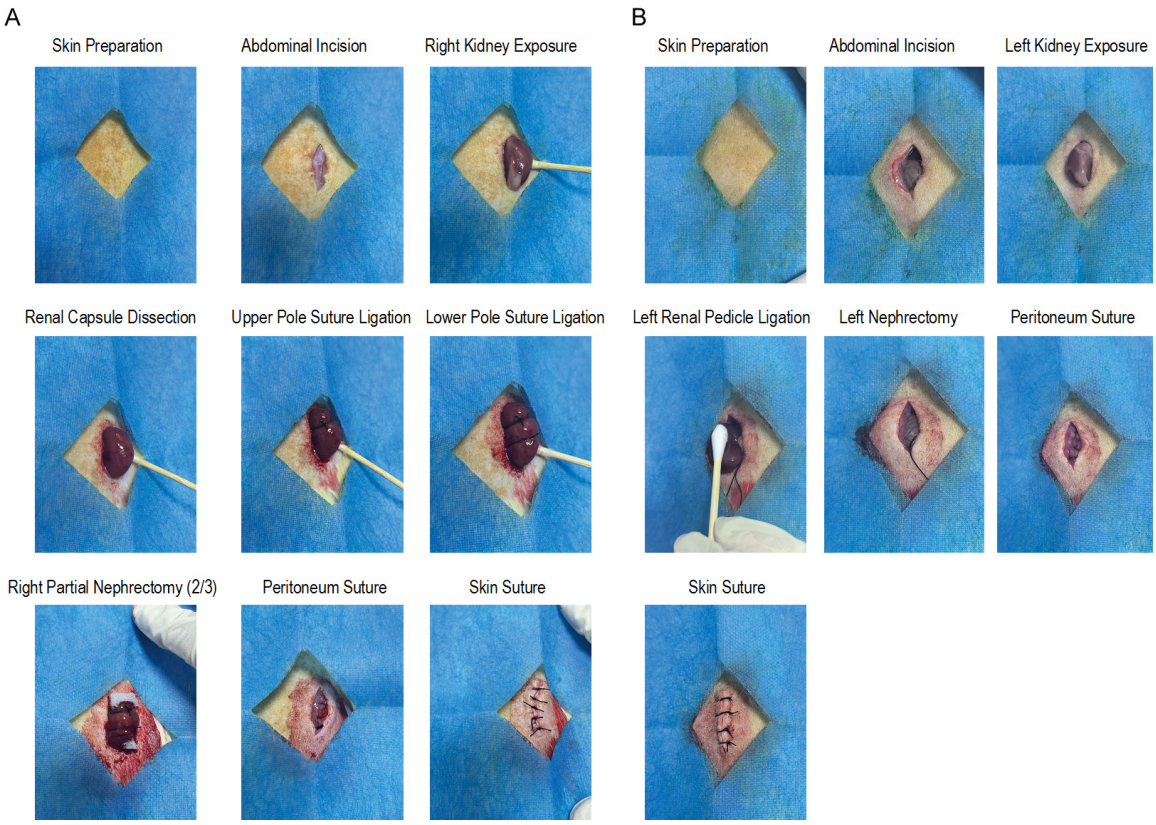


Figure 1. Surgical procedures for 5/6 nephrectomy in rats. A. Right bipolar nephrectomy (first surgery): Skin preparation, abdominal incision, right kidney exposure, renal capsule dissection, upper pole suture ligation, lower pole suture ligation, right partial nephrectomy (2/3), peritoneum suture, and skin suture. B. Left total nephrectomy (second surgery): Skin preparation, abdominal incision, left kidney exposure, left renal pedicle ligation, left nephrectomy, peritoneum suture, and skin suture.

4 weeks. All groups received a high-phosphate (1.2%) diet during the intervention period.

Animal model

Male Sprague-Dawley rats (230 ± 20 g) were purchased from Spebo (Beijing) Biotechnology Co., Ltd. (license number: SCXK [Jing] 2024-0001). Rats were housed in SPF conditions at 22 ± 1°C, 50 ± 5% humidity, with a 12/12 h light-dark cycle. A two-step surgical procedure was performed to establish the 5/6 nephrectomy model in rats [20]. The 5/6 nephrectomy rat maintained on a high-phosphate diet represents a well-established model of human SHPT [21]. In the first surgical step (**Figure 1A**), rats were anesthetized and dorsal fur was shaved. The abdomen was opened through a layer-by-layer incision of skin, muscle, and peritoneum. The right kidney was exteriorized, and the renal capsule was dissected. The upper and lower poles were ligated with 3-0 silk suture until tissue blanching, then excised with a scalpel. Hemostasis was achieved by compression. The peritoneum and skin were sutured closed. One week later, the left kidney was exteriorized (**Figure 1B**). The left kidney was exteriorized through the same incision. After ligation of the renal artery, vein, and ureter with 3-0 silk, the kidney was removed. The peritoneum and skin were sutured. After surgery, three rats were given a high-phosphate diet (1.2%) for 4 weeks; three sham-operated rats received a normal-phosphate diet (0.8%). Both diets (Keao Xieli [Tiansu] Feed Co., Ltd.; SCXK [Jin] 2025-0003) were standardized for calcium (1.0%), vitamin D (750 IU/kg), lipids, and other nutrients. Four weeks later, rats were euthanized with sodium pentobarbital (50 mg/kg). Blood was sampled for creatinine, BUN, calcium, phosphorus, and iPTH measurements. Parathyroid glands were rapidly isolated under microdissection. All procedures were completed within one day.

Analysis of differentially expressed genes

The GSE75886 series matrix file used in this study was obtained from the NCBI GEO public database. This dataset contains samples from 13 hemodialysis patients, including 5 cases of diffuse parathyroid hyperplasia and 8 cases of nodular hyperplasia. Through differential expression analysis (with thresholds set at $P < 0.05$ and $|\log_2 FC| > 0.8$), DEGs were preliminarily identified from the GEO dataset. The candidate gene set was then subjected to topological analysis based on the protein-protein interaction (PPI) network. Specifically, DEGs were mapped to the STRING database to construct a global PPI network, thereby revealing potential regulatory relationships among genes. To further identify hub genes in the network, three graph-theoretic centrality metrics implemented in the cytoHubba plugin of Cytoscape - Degree (quantifying node connectivity), Betweenness centrality (quantifying the bridging capacity of nodes as information intermediaries), and Maximal Clique Centrality (MCC; quantifying the coreness of nodes within locally dense connected regions) - were applied to evaluate the topological importance of each node in the PPI network. The top 20 genes ranked by each metric were selected as candidate hub gene sets, and the intersection of the three sets was visualized using a Venn diagram for subsequent in-depth analysis.

Enrichment analysis

Based on Gene Ontology (GO) [22] and Kyoto Encyclopedia of Genes and Genomes (KEGG) databases [23], functional enrichment analysis was performed on the DEGs identified from the NHD versus DHD comparison in the GSE75886 dataset using the clusterProfiler [24] package. Significantly enriched terms in biological process (BP), cellular component (CC), molecular function (MF), and KEGG pathways were identified with an adjusted P-value < 0.05 as the significance threshold.

ROC curve analysis

To evaluate the diagnostic efficacy of the key hub genes in distinguishing diffuse from nodular parathyroid hyperplasia in hemodialysis patients, receiver operating characteristic (ROC) curves were constructed for each hub gene using its expression level in the GSE75886 dataset as the test variable and the hyperplasia pattern (NHD vs DHD) as the state variable. The area under the curve (AUC) was calculated to assess discriminatory performance. An AUC > 0.9 was considered to indicate high diagnostic value, while $0.7 < AUC \leq 0.9$ indicated moderate diagnostic value.

Biochemical assays

Serum creatinine (Cr), blood urea nitrogen (BUN), calcium, and phosphorus levels were measured using commercial colorimetric assay kits (Solarbio, Beijing, China; cat. nos. BC4910, BC1535, BC0720, and BC1655, respectively) according to the manufacturer's instructions. Intact parathyroid hormone (iPTH) was determined using a rat-specific competitive ELISA kit (Jianglai Bio, Shanghai, China; cat. no. JL21082) with a detection range of 3.12-200 pg/mL. All absorbance readings were performed on a microplate reader at the specified wavelengths (Cr: 505 nm; BUN: 630 nm; calcium: 520 nm; phosphorus: 660 nm; iPTH: 450 nm). These biochemical parameters were assessed in both Experiment 1 (sham vs. SHPT model) and Experiment 2 (SHPT model, SHPT + IBR2 low-dose, SHPT + IBR2 high-dose, and SHPT + cinacalcet groups) to evaluate renal function and mineral metabolism.

Histological staining

Paraffin-embedded parathyroid tissue sections (5 μm) were dewaxed, rehydrated, and stained with hematoxylin (Sigma, H3136) for 5 min. After differentiation (Servicebio, G1039) for 1-2 s and rinsing, sections were counterstained with eosin (Servicebio, G1001) for 1-2 min, dehydrated, cleared, and mounted with neutral balsam (Servicebio, WG10004160). Slides were scanned using a panoramic scanner (Pannoramic MIDI, 3DHISTECH). H&E staining was conducted, and the sections were examined under light microscopy by two certified pathologists. For IHC, sections were deparaffinized, rehydrated, and microwave-treated in 1× Tris-EDTA buffer (pH 9.0, Servicebio, G1203) for 20 min to retrieve antigens. After blocking endogenous peroxidase with H_2O_2 (ZSGB-Bio, PV-9000, reagent 1) for 30 min and 5% goat serum (ZSGB-Bio, ZLI-9021) containing 0.3% Triton X-100 for 1 h, sections were incubated overnight at 4°C with primary antibodies diluted in 2% goat serum: Ki-67 (1:200, Proteintech, 28074-1-AP)

Table 1. Primer sequences for qRT-PCR

Sequence	Name	Length (bp)
CTGGAGAAGAGCTATGAG	*β-actin*-F	141
GATGGAATTGAATGTAGTTTC	*β-actin*-R	
CAGTACAACTCCATGACCAG	*Sox2*-F	75
CTGCTGCGAGTAGGACAT	*Sox2*-R	
AGAACAGGGTATGATAAC	*Bcl2*-F	94
AGTCTTCATCTCCAGTAT	*Bcl2*-R	
CCTTGTGGGTCTGTTTGA	*H3C13*-F	75
ATGTCCTTGGGCATGATG	*H3C13*-R	
GAAGTTCTTGGCTATTAC	*Ctnnb1*-F	122
TGTAGGTTCTCATTATGT	*Ctnnb1*-R	
AGCAGGTGAAGAATGATT	*IL10*-F	83
GCAGTTGATGAAGATGTC	*IL10*-R	
TGGTAAAGGTGGTAAAGG	*H4C6*-F	79
GATGCCCTGGATATTGTC	*H4C6*-R	
TTACAGAACAGACTACTCAG	*Rad51*-F	80
GAAGCAGCATCCTTAGAA	*Rad51*-R	
ACAGTTGACGAGACATAT	*Alb*-F	97
TTATCTGCTTCTCCTTGT	*Alb*-R	

or RAD51 (1:200, Bioss, bs-1221R). Following PBST washes, sections were incubated sequentially with reaction enhancer (ZSGB-Bio, PV-9000, reagent 2) at 37°C for 30 min and HRP-conjugated goat anti-rabbit IgG polymer (ZSGB-Bio, PV-9000, reagent 3) at 25°C for 1 h. DAB (ZSGB-Bio, ZLI-9019) was applied for 3-5 min, followed by hematoxylin counterstaining, differentiation, dehydration, clearing, and mounting. Positive expressions were observed as brown or brownish-yellow staining under a digital slide scanning system (WINMEDIC, Win10).

Quantitative image analysis of RAD51 and Ki-67 immunostaining

Image quantification was performed using ImageJ/Fiji (version 2.x; National Institutes of Health, Bethesda, MD, USA). RGB images were subjected to color deconvolution [25] using the Ruifrok-Johnston algorithm implemented in the Colour Deconvolution 2 plugin. The predefined settings/algorithm were applied to separate the composite RGB image into two independent grayscale channels: hematoxylin (nuclear counterstain) and DAB (immunoreactivity). All threshold parameters were kept constant throughout the same experimental batch. Background signals were verified using negative control sections (primary antibody replaced with PBS) to ensure objective and consistent threshold settings.

qRT-PCR

Total RNA was isolated from parathyroid specimens using TRIzol reagent (Life Technologies, 15596026) following the supplier's instructions. The concentration and purity of RNA were determined spectrophotometrically (EzDrop-1000, Blue-Ray). First-strand cDNA was reverse-transcribed from 2 μg of total RNA using the FastKing RT Kit (Tiangen, KR116) according to the manufacturer's guidelines. Quantitative PCR was performed on a QuantStudio 5 system (Applied Biosystems) using Taq Pro Universal SYBR qPCR Master Mix (Vazyme, Q712-02). The 10 μL reaction mixture comprised 5 μL of 2× SYBR Master Mix, 0.25 μL of forward and reverse primers (10 μM each), 1 μL of cDNA, and 3.5 μL of nuclease-free water. The cycling program began with an initial denaturation step at 95°C for 10 min, then 40 cycles of 95°C for 15 s and 60°C for 30 s. Product specificity was verified by melting curve analysis. Relative mRNA levels were quantified by the $2^{-\Delta\Delta Ct}$ method [26], normalized to β-actin. Primer sequences are provided in **Table 1**.

Western blot analysis

Parathyroid tissue samples (100 mg) were lysed in 400 μL RIPA lysis buffer (Beyotime, P0013B) using a bead mill at 70 Hz for 2 cycles of 1 min each, followed by incubation on ice for 20 min. After centrifugation at 12,000 rpm at 4°C for 10 min, protein concentration in the supernatants was determined using a spectrophotometer (EzDrop1000, Blue-Ray). Protein lysates (60 μg) were denatured in 5× SDS-PAGE loading buffer by boiling (10 min), resolved on 10% polyacrylamide gels, and electrotransferred to 0.45 μm PVDF membranes (200 mA, 1 h). After blocking in 5% BSA/TBST (1 h, room temperature), membranes were probed overnight at 4°C with primary antibodies targeting RAD51 (1:2000, Proteintech, 67024-1-Ig), cleaved caspase-3 (1:1000, Proteintech, 68773-1-Ig), phospho-H2AX (Ser139) (1:1000, Proteintech, 83307-2-RR), or β-actin (1:4000, ZSGB-Bio, TA-09). Following TBST washes, blots were incubated with HRP-conjugated goat anti-mouse or anti-rabbit IgG (1:4000, Abmart) for 2 h at room temperature. Immunoreactive

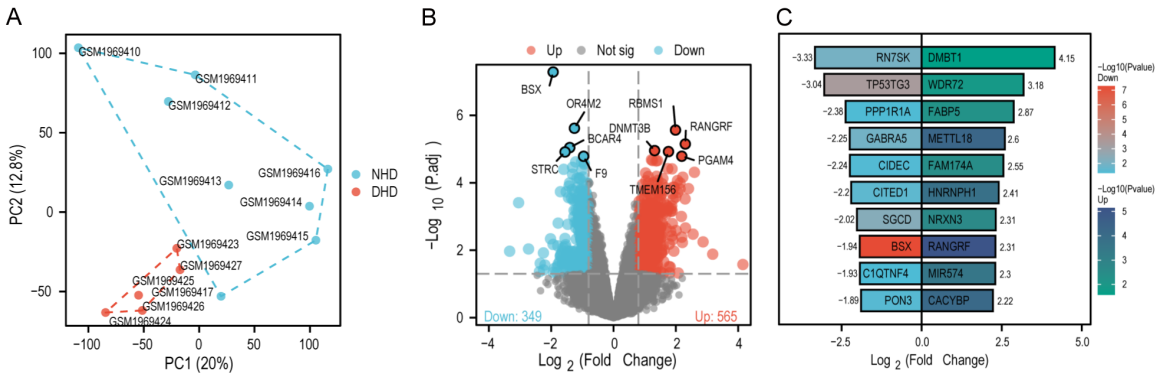


Figure 2. Differential expression analysis between NHD and DHD groups. A. Principal component analysis (PCA) was performed on the normalized expression data. B. Volcano plot showing 914 DEGs detected by limma analysis (|$\log_2$ fold change (FC)| > 0.8, $P < 0.05$), comprising 565 up-regulated (red) and 349 down-regulated (blue) genes. Genes without significant differential expression were displayed in gray. C. Bidirectional bar chart displaying the top 20 DEGs ranked by absolute $\log_2$FC. NHD: nodular hyperplasia, DHD: diffuse hyperplasia.

bands were detected by ECL chemiluminescence (Millipore, WBKLS0100) and imaged on a Tanon 5200Multi system.

Statistical analysis

GraphPad Prism (v. 8.4.3) and R (v. 4.3.1) were employed for statistical processing. Normality was tested using the Shapiro-Wilk method. Comparisons between two groups were analyzed using unpaired Student's *t*-test, whereas comparisons among multiple groups were first analyzed using one-way ANOVA and then evaluated using Tukey's multiple comparisons test. As a complementary robustness assessment, effect sizes (Cohen's *d*) were additionally calculated. Statistical significance was defined as $P < 0.05$.

Results

Identification of DEGs

Principal component analysis (PCA) of the normalized expression profiles showed that PC1 and PC2 accounted for 20.0% and 12.8% of the total variance, respectively, with a cumulative proportion of 32.8%. The PCA plot showed partial separation between the NHD and DHD groups along PC1, with no obvious outliers detected (**Figure 2A**). A total of 914 DEGs were identified between NHD and DHD groups using limma analysis with the criteria of |Log_2FC| > 0.8 and $P < 0.05$, comprising 565 upregulated and 349 downregulated genes (**Figure 2B**). The bidirectional bar chart displays the top 20 DEGs, comprising 10 upregulated and 10 downregulated genes (**Figure 2C**). Among the upregulated genes, DMBT1 showed the most pronounced upregulation ($\log_2$FC = 4.15, P = 0.0265), followed by WDR72 ($\log_2$FC = 3.18), FABP5 ($\log_2$FC = 2.87), and METTL18 ($\log_2$FC = 2.60, $P = 4.89 \times 10^{-5}$). Among the downregulated genes, RN7SK exhibited the greatest downregulation ($\log_2$FC = -3.33, P = 0.0107), followed by TP53TG3 ($\log_2$FC = -3.04, $P = 3.90 \times 10^{-4}$) and PPP1R1A ($\log_2$FC = -2.38).

Enrichment analysis of DEGs

We performed GO enrichment analysis on 914 DEGs and identified 30 significantly enriched terms ($P < 0.05$) (**Figure 3A**). At the cellular component level, the enriched terms mainly included collagen trimer and the beta-catenin destruction complex, with *CTNNB1* as a core hub gene. Biological processes were dominated by DNA replication regulation, DNA damage response, and mitochondrial outer membrane permeabilization. Molecular functions were highlighted by DNA damage sensor activity, with *RAD51* confirmed as the core gene in this category. Notably, multiple hub genes, including *CTNNB1*, *RAD51*, and *IL10*, were simultaneously involved in several functional modules, suggesting their potential cross-regulatory roles in SHPT pathogenesis. KEGG enrichment analysis revealed 20 significantly enriched pathways ($P < 0.05$) (**Figure 3B**). Among these, ferroptosis showed the most significant enrichment, involving VDAC2, GCLM, and TFRC; nonhomologous end-joining exhibited the highest

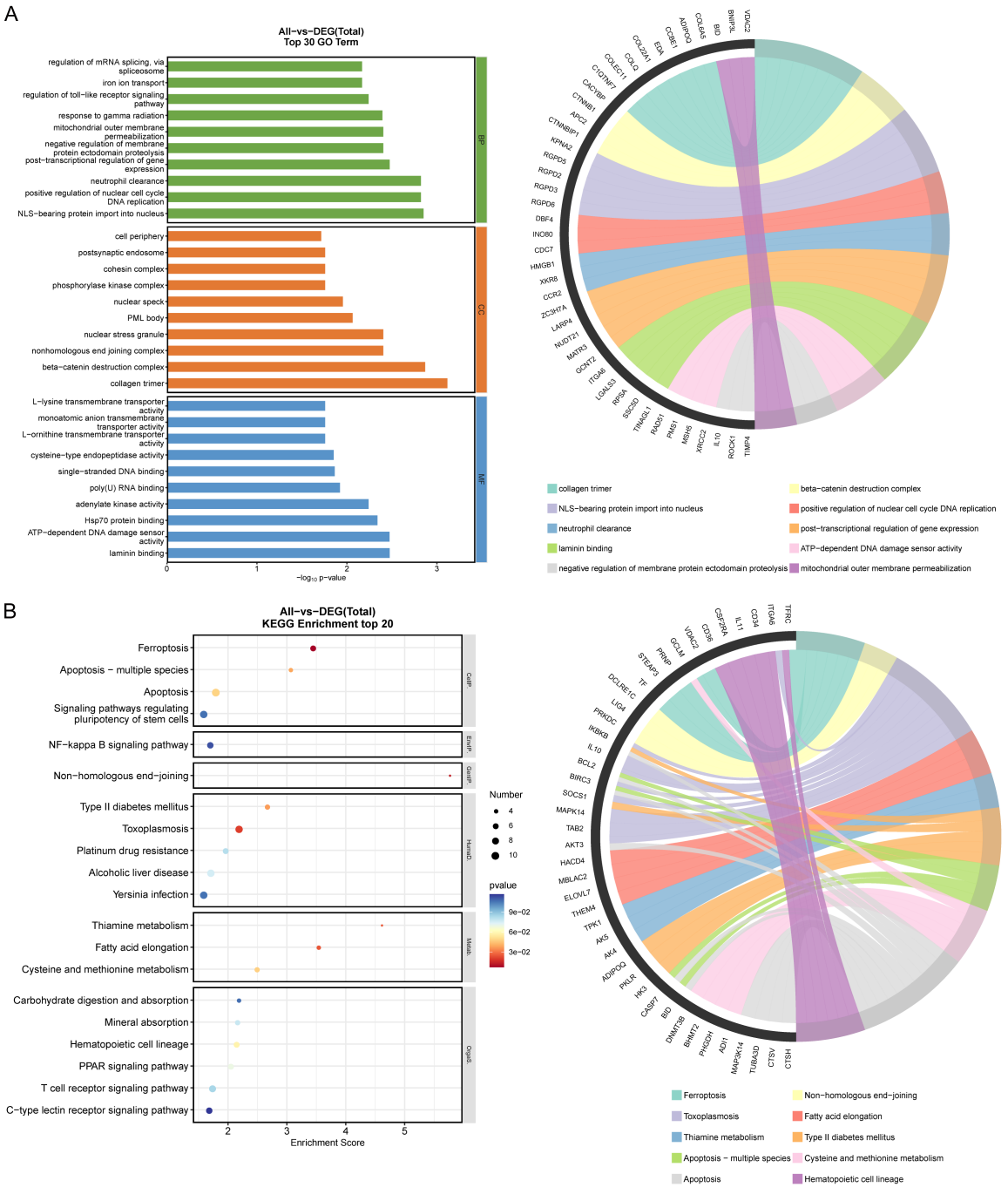

A
All−vs−DEG(Total)
Top 30 GO Term
regulation of mRNA splicing, via spliceosome
iron ion transport
regulation of toll−like receptor signaling pathway
response to gamma radiation
mitochondrial outer membrane permeabilization
negative regulation of membrane protein ectodomain proteolysis
post−transcriptional regulation of gene expression
neutrophil clearance
positive regulation of nuclear cell cycle DNA replication
NLS−bearing protein import into nucleus
cell periphery
postsynaptic endosome
cohesin complex
phosphorylase kinase complex
nuclear speck
PML body
nuclear stress granule
nonhomologous end joining complex
beta−catenin destruction complex
collagen trimer
L−lysine transmembrane transporter activity
monoatomic anion transmembrane transporter activity
L−ornithine transmembrane transporter activity
cysteine−type endopeptidase activity
single−stranded DNA binding
poly(U) RNA binding
adenylate kinase activity
Hsp70 protein binding
ATP−dependent DNA damage sensor activity
laminin binding
BP
CC
MF
−log10 p−value
collagen trimer
beta−catenin destruction complex
NLS−bearing protein import into nucleus
positive regulation of nuclear cell cycle DNA replication
neutrophil clearance
post−transcriptional regulation of gene expression
laminin binding
ATP−dependent DNA damage sensor activity
negative regulation of membrane protein ectodomain proteolysis
mitochondrial outer membrane permeabilization
B
All−vs−DEG(Total)
KEGG Enrichment top 20
Ferroptosis
Apoptosis − multiple species
Apoptosis
Signaling pathways regulating pluripotency of stem cells
NF−kappa B signaling pathway
Non−homologous end−joining
Type II diabetes mellitus
Toxoplasmosis
Platinum drug resistance
Alcoholic liver disease
Yersinia infection
Thiamine metabolism
Fatty acid elongation
Cysteine and methionine metabolism
Carbohydrate digestion and absorption
Mineral absorption
Hematopoietic cell lineage
PPAR signaling pathway
T cell receptor signaling pathway
C−type lectin receptor signaling pathway
CellP
EnvIP
GenIP
HumanD
Metab.
OrgaS
Enrichment Score
Number
pvalue
Ferroptosis
Non−homologous end−joining
Toxoplasmosis
Fatty acid elongation
Thiamine metabolism
Type II diabetes mellitus
Apoptosis − multiple species
Cysteine and methionine metabolism
Apoptosis
Hematopoietic cell lineage
C
SMID Breast Cancer Basal Dn
HAMAI Apoptosis Via Trail Up
[Reactome] Infectious Disease
ONKEN Uveal Melanoma Up
NABA Matrisome
[Reactome] Viral Infection Pathways
MILI Pseudopodia Haptotaxis Up
DIAZ Chronic Myelogenous Leukemia Up
HSIAO Housekeeping Genes
SHEN SMARCA2 Targets Up
NES = −2.307
P value < 0.001
NES = 2.253
P value < 0.001
NES = 2.313
P value < 0.001
NES = 2.276
P value < 0.001
NES = −2.304
P value < 0.001
NES = 2.349
P value < 0.001
NES = 2.353
P value < 0.001
NES = 2.343
P value < 0.001
NES = 2.562
P value < 0.001
NES = 2.632
P value < 0.001
D
Mrna Metabolic Process
Mrna Processing
Microtubule Based Process
Microtubule Cytoskeleton Organization
Nucleoside Triphosphate Metabolic Process
Microcephaly
PML Body
Transcription Factor Binding
RNA Polymerase Ii Specific DNA Binding Transcription Factor Binding
DNA Binding Transcription Factor Binding
NES = 2.190
P value < 0.001
NES = 2.156
P value < 0.001
NES = 2.186
P value < 0.001
NES = 2.168
P value < 0.001
NES = 2.230
P value < 0.001
NES = 2.212
P value < 0.001
NES = 2.311
P value < 0.001
NES = 2.406
P value < 0.001
NES = 2.432
P value < 0.001
NES = 2.538
P value < 0.001

Figure 3. Functional enrichment and diagnostic analysis of DEGs in SHPT. A. GO enrichment analysis of 914 DEGs. Left: The top 30 significantly enriched GO terms ($P < 0.05$). Right: Chord diagram illustrating the associations between hub genes. B. KEGG pathway enrichment analysis. Left: Dot plot showing the top 20 significantly enriched KEGG pathways ($P < 0.05$), with dot size scaled by gene number and color coded by adjusted *p*-value. Right: Chord diagram depicting multi-to-multi correspondences between core genes and pathways. C. GSEA C2 pathway analysis identifying 10 significantly enriched pathways. D. GO enrichment analysis by GSEA.

enrichment score, involving DNA repair genes LIG4 and PRKDC; and apoptosis-related pathways were also significantly enriched, with BCL2 as the hub gene.

We conducted Gene Set Enrichment Analysis (GSEA) on the C2 (curated pathways) and C5 (Gene Ontology) gene sets from the MSigDB database. Gene sets with |NES| > 1 and $P < 0.05$ were considered significantly enriched. C2 pathway analysis identified 10 significantly enriched pathways (**Figure 3C**). The *SMARCA2* target gene set (SHEN_SMARCA2_TARGETS_UP) showed the strongest enrichment signal ($P = 0.0026$), followed by the housekeeping gene set (HSIAO_HOUSEKEEPING_GENES) ($P = 0.0026$). Positive enrichment was also observed in the chronic myelogenous leukemia upregulated gene set ($P = 0.0071$), pseudopodia haptotaxis-related gene set ($P = 0.015$), and TRAIL-mediated apoptosis pathway ($P = 0.017$), whereas negative enrichment was found in the NABA matrisome ($P = 0.015$) and basal-type breast cancer downregulated gene set ($P = 0.017$). GO enrichment analysis (**Figure 3D**) revealed significant enrichment in DNA-binding transcription factor binding ($P = 0.016$), with core genes including *MIXL1*, *HMGB1*, *PIAS2*, *PRKDC*, *CTNNB1*, *NCOA1*, *MAX*, and *SP3*.

PPI network construction and hub gene identification

Protein-protein interaction network analysis of the candidate genes was conducted using Cytoscape software. The resulting PPI network comprised 641 nodes and 2,118 edges, with an average degree of 6.61 (**Figure 4A**). To identify the most robust hub genes, three network centrality measures - Degree, Betweenness, and MCC (Maximal Clique Centrality) - were applied, and the top 20 genes from each measure were extracted. Venn diagram analysis of the three gene sets revealed 8 core hub genes commonly shared by all three measures: *CTNNB1, ALB, BCL2, H3C13, H4C6, RAD51, IL10*, and *SOX2* (**Figure 4B**).

ROC curve analysis of key genes for diagnostic prediction

To test the discriminative ability of the screened key genes as potential biomarkers, we performed ROC curve analysis (**Figure 5**). The results showed that both *H3C13* and *RAD51* achieved an AUC of 1.000, indicating that these two genes can excellently distinguish diffuse from nodular hyperplasia. They are thus considered the most promising candidate biomarkers identified in this study. *CTNNB1* (AUC = 0.975) and *H4C6* (AUC = 0.925) also exhibited excellent discriminatory capacity, while IL10 (AUC = 0.900) reached a good level, and *SOX2* (AUC = 0.875), *ALB* (AUC = 0.850), and *BCL2* (AUC = 0.850) all showed favorable classification performance. Collectively, these findings indicate that all eight key genes possess high predictive value and may represent potential biomarkers for disease onset and progression.

Validation of the rat SHPT model

H&E staining revealed that parathyroid glands from the sham-operated group exhibited normal architecture, with chief cells arranged in regular cords, moderate cellularity, and abundant stromal tissue. Conversely, the model group showed marked parathyroid hyperplasia, as evidenced by increased cellularity, disorganized trabecular patterns, and diminished interstitial stroma (**Figure 6A**). Ki-67 immunohistochemistry revealed that nuclei in the sham group were predominantly counterstained with hematoxylin, with negligible DAB-positive signals, resulting in a Ki-67 positivity rate of 0.08 ± 0.10% (**Figure 6B**). In the model group, extensive brown DAB-positive nuclear staining was observed, and the Ki-67 index was significantly elevated to 20.62 ± 2.99% ($P < 0.001$). Serum PTH was markedly elevated in the model group (172.4 ± 22.7 vs. 29.6 ± 5.5 pg/mL) relative to sham-operated rats, confirming the successful establishment of the SHPT model. This was accompanied by impaired renal function, as evidenced by significantly increased serum creatinine and BUN levels, together with disturbed

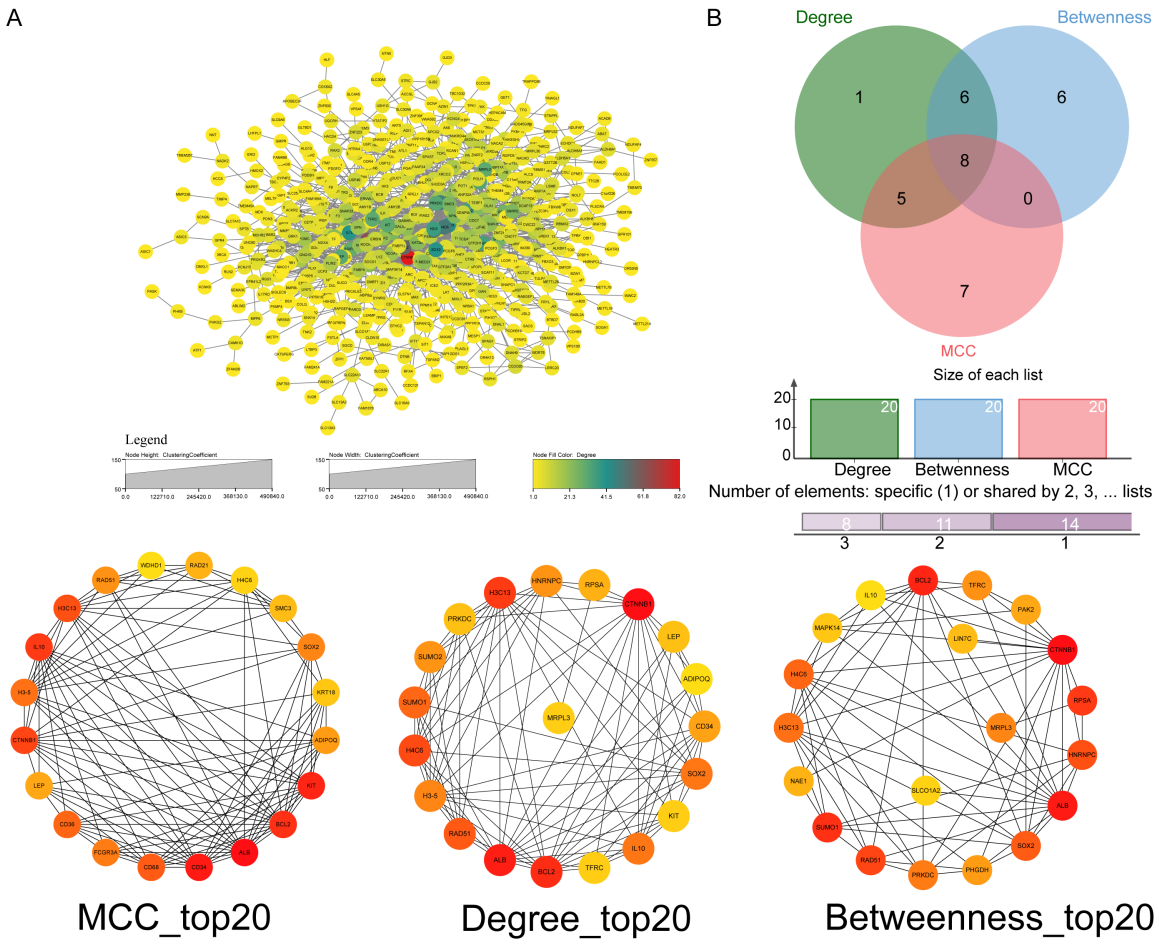


Figure 4. PPI network construction and hub gene identification of DEGs in SHPT. A. Protein-protein interaction (PPI) network of 914 candidate DEGs constructed and visualized in Cytoscape (641 nodes, 2,118 edges, mean node degree = 6.61). B. Venn diagram (upper) and intersection bar chart (lower) comparing the top 20 hub genes ranked by three network centrality metrics: Maximal Clique Centrality (MCC), Degree centrality, and Betweenness centrality. The lower panels show the top 20 hub genes identified by each centrality metric, respectively. Node size and color intensity are proportional to the centrality score.

mineral metabolism characterized by significantly decreased serum calcium and elevated phosphorus (all $P < 0.05$; **Figure 6C**).

Candidate gene validation in a rat model

The SHPT model group exhibited significantly altered expression of seven candidate genes compared with the sham group (**Figure 7**). Notably, *Rad51* exhibited the most pronounced upregulation, with a relative expression of 6.257 ± 1.149 versus 1.065 ± 0.211 in the sham group (approximately 5.87-fold, $P < 0.01$). *H3c13* (3.924 ± 0.526, $P < 0.01$) and *IL10* (2.881 ± 0.242, $P < 0.001$) were also markedly upregulated. Additionally, *Ctnnb1*, *H4c6*, and *Alb* were significantly upregulated by approximately 2-fold (all $P < 0.01$), whereas *Bcl2* showed mild upregulation (1.50-fold, $P < 0.05$). *Sox2* was the only downregulated gene (0.693 ± 0.037 vs. 0.950 ± 0.132, $P < 0.05$). Based on its greatest fold change, statistical significance, and consistent high expression across all model samples (5.43-7.57-fold), *Rad51* was selected as the core target for subsequent in-depth investigation.

RAD51 inhibition attenuates parathyroid hyperplasia in SHPT rats

Western blot analysis demonstrated that RAD51 protein levels were markedly elevated in the parathyroid glands of SHPT model rats relative to the sham group (2.393 ± 0.088 vs. 1.000 ± 0.251, $P < 0.001$) (**Figure 8A**). The original uncropped western blot images

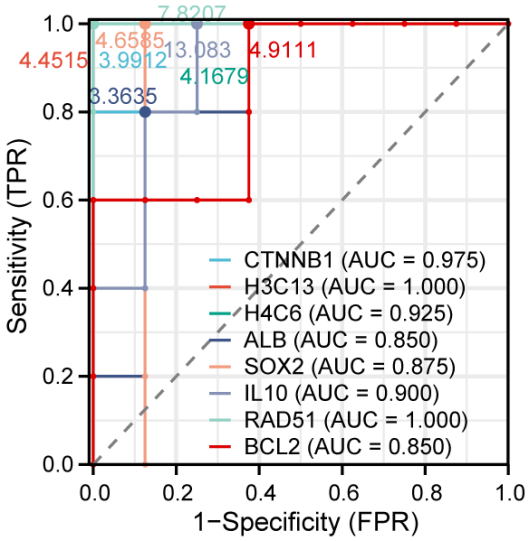


Figure 5. ROC curves for the hub genes. AUC values were as follows: both *H3C13* and *RAD51* achieved an AUC of 1.000, *CTNNB1* (0.975), *H4C6* (0.925), *IL10* (0.900), *SOX2* (0.875), and *ALB* and *BCL2* (both 0.850). AUC, area under the curve; ROC, receiver operating characteristic.

corresponding to **Figure 8A** are provided in Supplementary Figures 1, 2. Immunohistochemical staining further localized this upregulation to parathyroid cell nuclei, with the RAD51-positive rate markedly elevated in the model group (90.08 ± 12.01% vs. 0.41 ± 0.38% in the sham group, $P < 0.05$) (**Figure 8B**). Histopathological examination by H&E staining showed that low-dose IBR2 treatment resulted in modest amelioration, with moderately reduced cellularity and partial restoration of cord-like architecture. High-dose IBR2 produced substantial histopathological improvement, with markedly reduced cellularity approaching normal levels, predominant cord-like patterns, and restored stromal-vascular networks. The cinacalcet-treated group showed comparable improvement to the high-dose IBR2 group, characterized by reduced cellularity and restored architectural patterns (**Figure 8C**). To assess the effect of RAD51 inhibition on parathyroid cell proliferation, immunohistochemical staining for the cell proliferation marker Ki-67 was performed to evaluate the proliferative activity of parathyroid cells in each group. Compared with the model group, the Ki-67-positive rate was significantly reduced following treatment, decreasing to 5.55 ± 3.97% in the low-dose IBR2 group (2 mg/kg) and 3.03 ± 3.09% in the high-dose IBR2 group (10 mg/kg). The cinacalcet-treated group (10 mg/kg) exhibited the lowest Ki-67-positive rate at 0.68 ± 0.61% (**Figure 8C**). Collectively, these findings indicate that RAD51 inhibition effectively attenuates parathyroid cellular hyperplasia in SHPT, with a trend toward greater efficacy at higher doses.

Therapeutic effects of RAD51 inhibition on serum biochemical parameters in SHPT

To evaluate the therapeutic potential of RAD51 inhibition in SHPT, we next examined the effects of IBR2 on serum biochemical parameters in SHPT rats (**Figure 9**). One-way ANOVA showed significant differences in serum PTH ($P < 0.0001$), creatinine ($P = 0.0036$), phosphorus ($P = 0.0004$), and calcium ($P = 0.0068$), whereas BUN did not differ ($P = 0.233$). IBR2 dose-dependently reduced serum PTH (low-dose: 137.56 ± 11.27 pg/mL, 23.2%, $P = 0.037$; high-dose: 83.14 ± 8.47 pg/mL, 53.6%, $P = 0.002$) versus the SHPT model group (179.08 ± 22.42 pg/mL), with efficacy comparable to cinacalcet (57.48 ± 13.46 pg/mL, 67.9%, $P < 0.0001$). IBR2 also restored serum calcium (low-dose: 19.50 ± 0.62 μmol/dL, +31.3%, $P = 0.052$; high-dose, 20.34 ± 2.09 μmol/dL, +36.9%, $P = 0.024$), whereas cinacalcet was ineffective ($P > 0.99$). All treatments lowered serum phosphorus to varying degrees, with cinacalcet showing the strongest effect (46.8%, $P < 0.001$), followed by IBR2 high-dose (25.2%, $P = 0.013$) and low-dose (18.1%, $P = 0.066$). However, only cinacalcet improved renal function by lowering creatinine (18.1%, $P = 0.021$); IBR2 had no significant effect ($P = 0.392$), and neither drug affected BUN.

RAD51 regulates DNA damage repair and apoptosis in SHPT parathyroid tissue

To determine whether RAD51 suppression disrupts DNA damage repair and promotes apoptosis in SHPT parathyroid tissue, we examined the protein expression of RAD51, γH2AX, and cleaved-caspase-3 following pharmacological RAD51 inhibition (**Figure 10A**). Compared with the SHPT model group, IBR2 dose-dependently reduced RAD51 protein levels (low dose: 0.62 ± 0.05, $P = 0.0006$; high dose: 0.35 ± 0.08, $P < 0.0001$), concomitantly increasing the DNA double-strand break marker γH2AX (low dose:

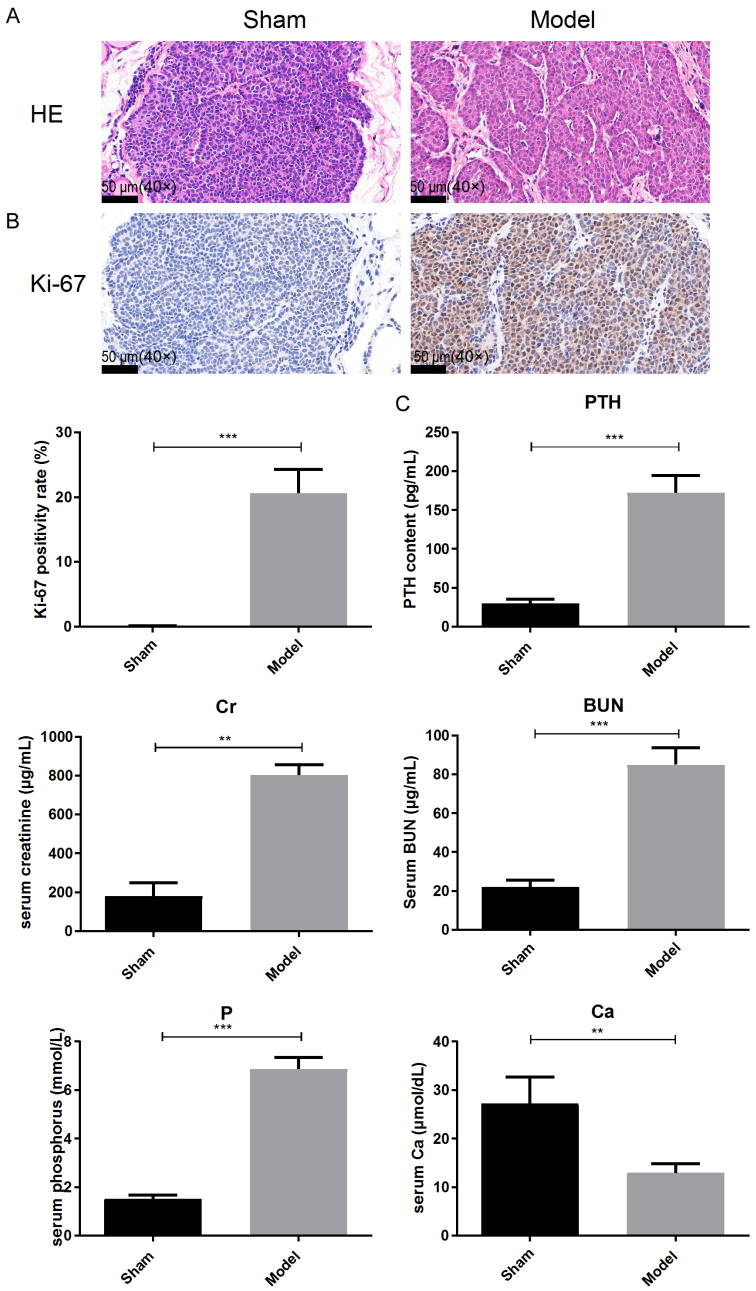


Figure 6. Biochemical and histopathological characterization of the rat SHPT model. A. Representative images of H&E staining of parathyroid tissues from the Sham and Model groups. B. Immunohistochemical detection of the cell proliferation marker Ki-67 (upper panels: representative images; magnification, 40×; scale bars, 50 μm), together with quantitative analysis of Ki-67-positive cells (lower panels). Brown nuclear staining indicates Ki-67-positive cells. C. Serum levels of parathyroid hormone (PTH), creatinine (Cr), blood urea nitrogen (BUN), phosphorus (P), and calcium (Ca) in the Sham and Model groups at 4 weeks. *$P < 0.05$, **$P < 0.01$ and ***$P < 0.001$ (unpaired Student's *t*-test).

2.18 ± 0.12, $P = 0.0007$; high dose: 2.88 ± 0.06, $P < 0.0001$) and the apoptosis marker cleaved-caspase-3 (low dose: 1.64 ± 0.19, $P = 0.048$; high dose: 2.69 ± 0.22, $P = 0.0001$). The positive control cinacalcet also reduced RAD51 (0.70 ± 0.10, $P = 0.0033$) and elevated cleaved-caspase-3 (1.79 ± 0.27, $P = 0.017$); however, it did not significantly affect γH2AX expression (1.15 ± 0.39, $P = 0.832$). Representative Western blot images of RAD51, cleaved-caspase-3, γH2AX, and β-actin are presented in **Figure 10B**. The original uncropped western blot images corresponding to **Figure 10B** are provided in Supplementary Figures 3, 4, 5, 6. These findings indicate that RAD51 inhibition attenuates DNA repair capacity and aggravates DNA damage burden, consequently inducing parathyroid cell apoptosis via a pathway mechanistically divergent from cinacalcet.

Discussion

Although bioinformatics analyses of the GSE75886 dataset have identified 914 differentially expressed genes between nodular and diffuse parathyroid hyperplasia in SHPT [15], the molecular underpinnings driving the transition from pharmacologically responsive diffuse hyperplasia to refractory nodular hyperplasia are not yet fully elucidated. Physiologically, parathyroid chief cells act as highly specialized calcium sensors, with membrane-bound CaSR detecting subtle changes in extracellular calcium and rapidly modulating PTH release, while VDR mediates 1,25-dihydroxyvitamin D-induced suppression of PTH gene transcription [27, 28]. Together with FGF23/FGFR1-Klotho signaling, these pathways collectively maintain parathyroid quiescence [29, 30]. In CKD, however, this homeostatic archi-

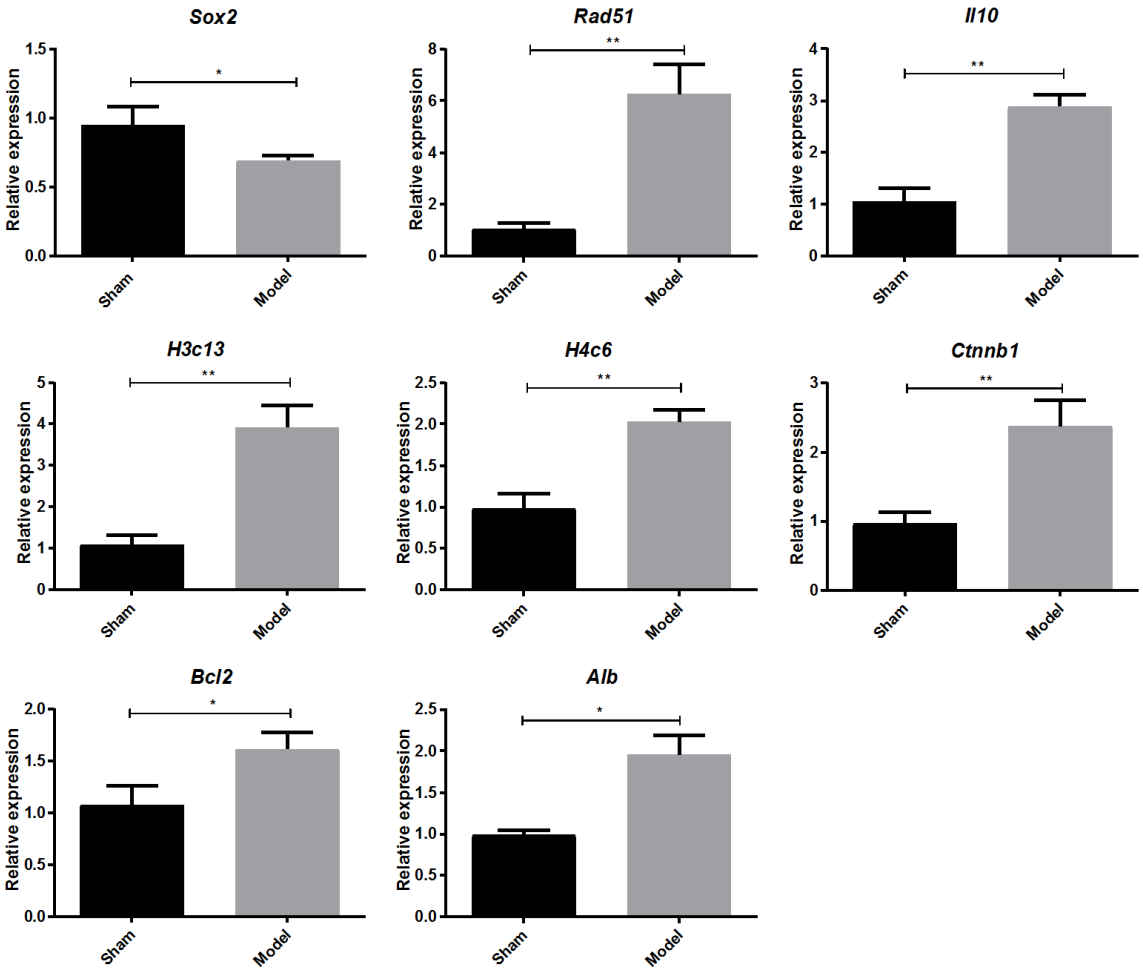


Figure 7. mRNA expression of candidate genes in parathyroid glands of SHPT rats. Relative mRNA expressions of *Sox2*, *Rad51*, *IL10*, *H3C13*, *H4C6*, *Ctnnb1*, *Bcl2*, and *Alb* in the Sham and Model groups. *$P < 0.05$, **$P < 0.01$ (unpaired Student's *t*-test).

tecture progressively collapses. Phosphate retention, 1,25D deficiency, and hypocalcemia impose chronic secretory drive, and with sustained hyperplasia, parathyroid expression of CaSR, VDR, and the FGF23 co-receptor Klotho is markedly downregulated - most prominently within hyperplastic nodules [27, 30-32]. The resulting receptor resistance creates a vicious cycle and entrenches refractoriness to calcimimetics and active vitamin D analogs. Because this therapeutic ceiling is determined by progressive loss of receptor expression at the glandular level - rather than by insufficient ligand availability - strategies targeting downstream intracellular networks may offer a mechanistically distinct route to controlling refractory disease [33, 34]. In this study, by applying complementary network centrality measures to the PPI network and extending functional validation to pharmacological intervention, we identify RAD51 as a robust biomarker and demonstrate that its pharmacological inhibition by IBR2 effectively attenuates parathyroid hyperplasia through DNA damage accumulation and apoptosis.

Our bioinformatic analysis identified eight hub genes with significant differential expression between nodular and diffuse hyperplasia. CTNNB1 encodes β-catenin, the central effector of canonical Wnt signaling [35], and aberrant β-catenin accumulation - driven by stabilizing mutations or epigenetic derepression of Wnt antagonists - has been documented in parathyroid adenomas and implicated in parathyroid carcinoma via EZH2-mediated

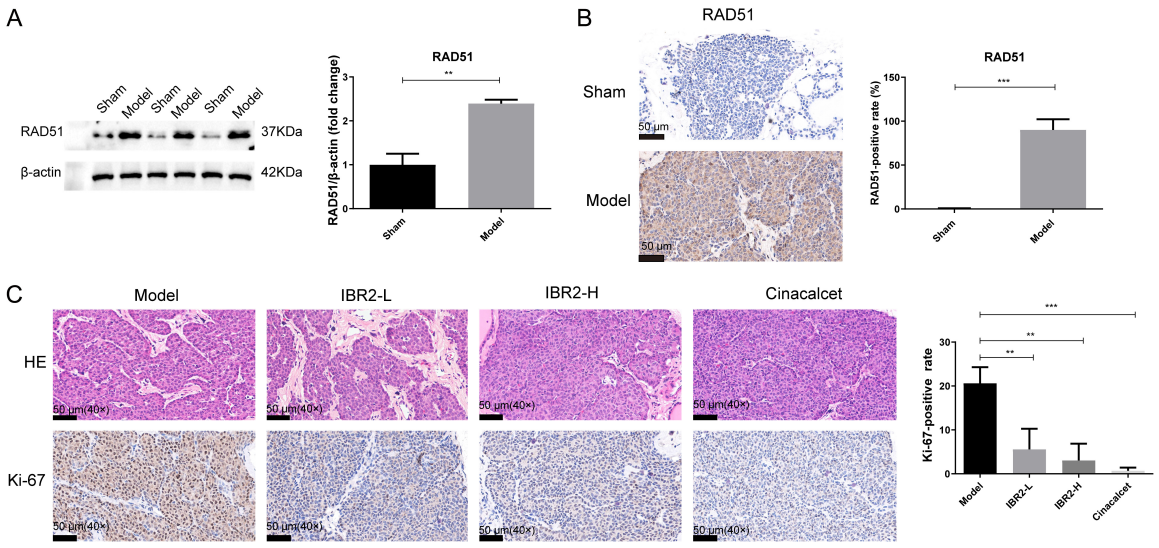


Figure 8. Effects of RAD51 inhibition on parathyroid cell proliferation and RAD51 expression in SHPT rats. A. Representative Western blot (left) and quantitative analysis (right) of RAD51 protein expression in parathyroid glands from the sham and model groups. B. Representative immunohistochemical staining (left) and quantification of positive cell rate (right) for RAD51 in parathyroid tissues. C. H&E staining (upper row) and Ki-67 immunohistochemical staining (lower row) of parathyroid sections across all experimental groups, with corresponding quantification of the Ki-67 positive cell rate (right). Magnification, 40×; Scale bars, 50 μm. $*P < 0.05$, $**P < 0.01$, $***P < 0.001$. (Two-group comparisons by unpaired Student's *t*-test; multi-group comparisons by one-way ANOVA followed by Tukey's post hoc test). IBR2-L, IBR2 low-dose group (2 mg/kg); IBR2-H, IBR2 high-dose group (10 mg/kg); Cinacalcet, cinacalcet-treated group (positive control).

H3K27me3 silencing of AXIN2 [36]. Björklund and colleagues found that 7.3% of spoRadic parathyroid adenomas contained a stabilizing mutation in exon 3 of CTNNB1, specifically the S37A mutation, which leads to resistance of β-catenin to ubiquitin-proteasomal degRadation [37]. More importantly, abnormal accumulation of unphosphorylated β-catenin as well as high expression of its target gene c-myc were observed in the hyperplastic parathyroid tissue associated with uremic secondary SHPT; this suggests that the persistent activation of the Wnt/β-catenin pathway is not only involved in the formation of adenomas but also serves as a key driver behind the transformation from diffuse hyperplasia to nodular hyperplasia in SHPT [38]. SOX2 has been reported as significantly upregulated in metastatic parathyroid carcinoma compared with non-metastatic lesions, forming part of a metastasis-specific gene signature alongside MMP9, CD24, and BMP7 [36]. Verdelli et al. reported nuclear SOX2 positivity in 18% of parathyroid adenomas; notably, SOX2-expressing cells retained the capacity for PTH secretion, suggesting preserved endocrine function [39]. However, it was the only hub gene downregulated in our rat model (0.693-fold). This result may reflect differences in disease stage: whereas SOX2 reactivation in human parathyroid tumors is predominantly observed in nodular hyperplasia and adenoma stages, the rat model in this study may still represent an early phase of diffuse hyperplasia. Histones are key proteins that regulate DNA compaction, and the coordinated upregulation of H3C13 and H4C6 (encoding H3.1 and H4, respectively) in the SHPT model reflects heightened histone demand in proliferating cells [40]. Although there are currently no direct studies on histone genes in parathyroid diseases, histone modifications such as H3K4me3 and H4K16ac play a significant role in the epigenetic upregulation of genes that regulate the cell cycle [41]. IL-10 and ALB are unlikely to function as direct local drivers of parathyroid cell proliferation; rather, they appear to exert indirect, systemic modulation of parathyroid function via immune-inflammatory and nutritional-metabolic pathways, respectively. Consequently, their altered expression may reflect overall CKD-MBD status rather than serve as direct molecular markers of hyperplasia [42, 43].

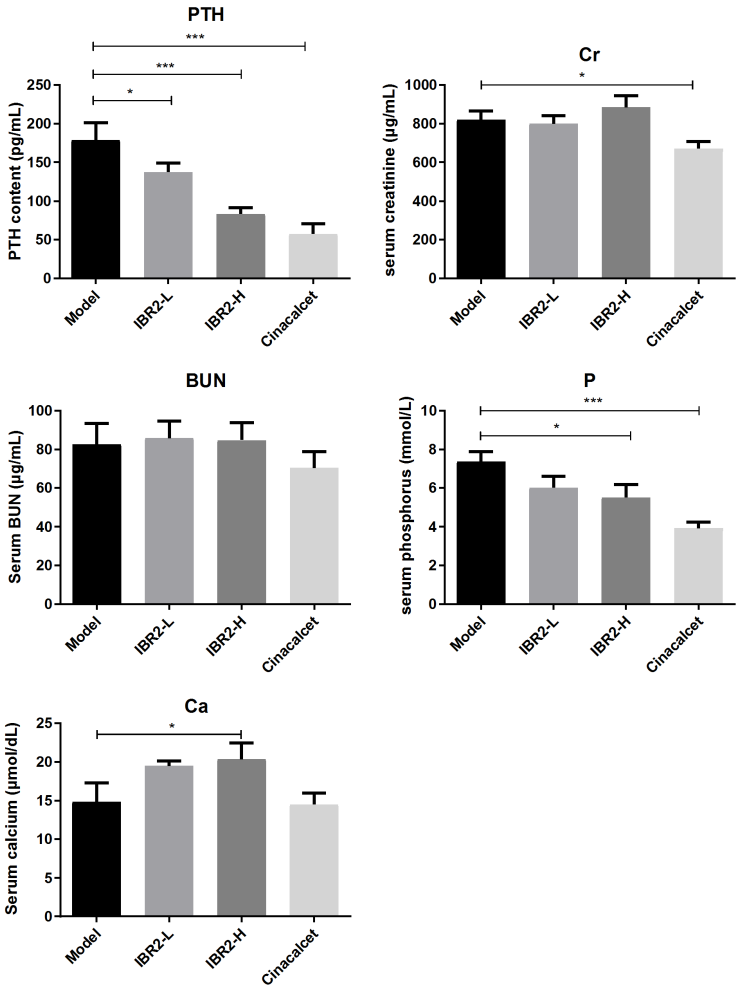


Figure 9. Serum biochemical parameters in the SHPT rat model. SHPT rats were treated with vehicle (Model), IBR2 (2 or 10 mg/kg), or cinacalcet (10 mg/kg) for 4 weeks, followed by measurement of serum parathyroid hormone (PTH), creatinine (Cr), blood urea nitrogen (BUN), phosphorus (P), and calcium (Ca). $*P < 0.05$, $**P < 0.01$, and $***P < 0.001$ (one-way ANOVA followed by Tukey's post hoc test).

Santamaría et al. [44] reported aberrant expression of DNA stability/repair genes and the cell cycle regulator CDC25C during diffuse-to-nodular parathyroid hyperplasia progression in SHPT. Our enrichment analysis corroborated and extended these findings. Of note, the genes identified in prior studies do not completely overlap with our screened key genes, which may be attributable to differences in analytical approaches, filtering criteria, and validation strategies. By integrating three network centrality measures (Degree, Betweenness, and MCC) with ROC curve assessment, we systematically identified eight key DEGs, all of which exhibited robust predictive performance and effectively distinguished SHPT occurrence and progression. Among the eight hub genes, RAD51 emerged as the most promising therapeutic target. As the key recombinase in the repair of double-strand breaks via homologous recombination [45, 46], RAD51 preserves genomic integrity by driving strand invasion, especially under high proliferation, averting unrepaired DSB accumulation [47, 48]. In the context of SHPT, the transition from polyclonal diffuse hyperplasia to monoclonal nodular hyperplasia requires sustained and accelerated cell cycle progression [49]. Early clonal analyses have established that diffuse hyperplasia in renal SHPT is polyclonal in origin, whereas nodular hyperplasia is characterized by monoclonal proliferation, indicating that nodular lesions display tumor-like growth properties [50, 51]. In the present study, parathyroid tissues from the SHPT model group exhibited marked cellular hyperplasia, accompanied by a significant increase in RAD51 protein expression. The data obtained herein reveal that under sustained proliferative pressure induced by uremic hyperphosphatemia, hypocalcemia, and secondary hormonal stimulation, parathyroid chief cells may maintain genomic integrity and evade apoptosis through RAD51-mediated homologous recombination repair (HR) and replication fork protection mechanisms. We propose that the feedback upregulation of RAD51 represents an adaptive response of parathyroid chief cells to replication stress and proliferative pressure [49], which may provide a favorable condition for the clonal expansion of drug-resistant nodular lesions. This speculation is supported by prior evidence from Santamaría et al. [44] of coordinated dysregulation of multiple DNA repair and stability genes in advanced SHPT. To test this hypothesis, we examined the function-

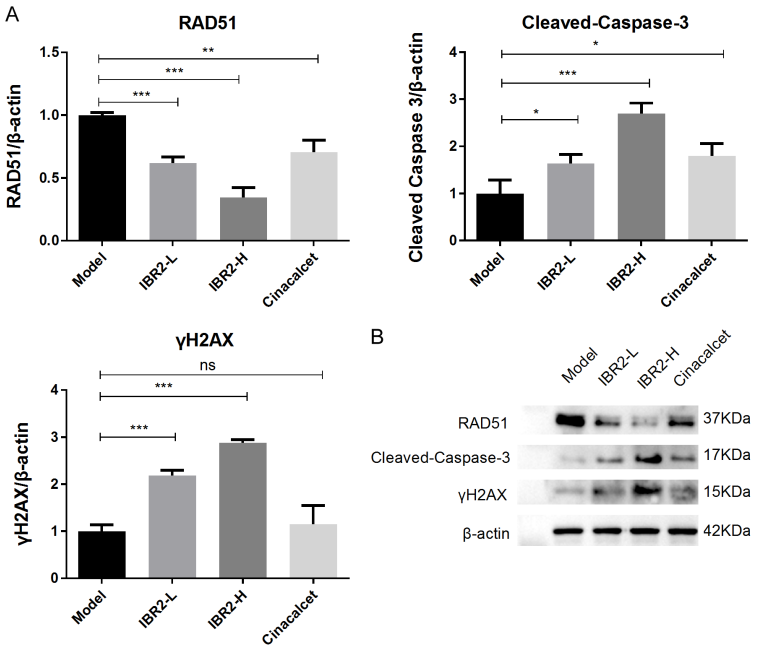


Figure 10. Effects of RAD51 inhibition on DNA damage repair and apoptosis in SHPT parathyroid tissue. A. Quantitative analysis of RAD51, cleaved-caspase-3, and γH2AX protein expression normalized to β-actin. B. Representative Western blot images showing protein bands of RAD51 (37 kDa), cleaved-caspase-3 (17 kDa), γH2AX (15 kDa), and β-actin (42 kDa). Model, secondary hyperparathyroidism model group; IBR2-L, low-dose IBR2 (2 mg/kg); IBR2-H, high-dose IBR2 (10 mg/kg); Cinacalcet, positive control (10 mg/kg). *$P < 0.05$, **$P < 0.01$, ***$P < 0.001$ (one-way ANOVA followed by Tukey's multiple comparisons test).

al consequences of RAD51 suppression in the SHPT rat model. Our results demonstrated that pharmacological inhibition of RAD51 markedly attenuated parathyroid hyperplasia through a defined molecular cascade: suppression of RAD51 compromised DNA repair via homologous recombination, resulting in the accumulation of unrepaired DSBs as evidenced by significant upregulation of γH2AX; this DNA damage burden in turn activated the intrinsic apoptotic pathway, reflected by increased cleaved-caspase-3 expression; the resulting apoptotic cell death reduced the total mass of parathyroid chief cells, which consequently lowered serum PTH levels and restored calcium-phosphorus homeostasis. IBR2 was originally identified by Zhu et al. as a compound that disrupts RAD51 self-assembly and accelerates its proteasome-mediated degRadation, thereby sensitizing cancer cells to DNA damage and apoptosis [52]. More recently, Pan et al. demonstrated that IBR2 reduces hepatocellular carcinoma cell proliferation, increases DNA damage (as evidenced by γH-2AX foci), and enhances apoptosis [53]. By contrast, the positive control cinacalcet, a CaSR agonist, reduces PTH secretion through receptor-mediated signaling without directly eliminating hyperplastic tissue [34]. Cinacalcet, a CaSR allosteric agonist, inhibits PTH gene transcription and secretion through downstream CaSR signaling, and enhances parathyroid cell-surface CaSR and VDR expression, thereby counteracting hormone resistance [54]. In the present study, γH2AX expression in the cinacalcet-treated group did not change significantly, indicating that cinacalcet does not exert its effects through the induction of DNA damage. Although cleaved-caspase-3 was mildly elevated and RAD51 protein levels slightly decreased in this group, these changes may be related to the indirect modulation of cell cycle and apoptotic pathways following CaSR activation.

However, the present study has some limitations. First, the sample sizes of both the bioinformatics analysis and the animal experiments were limited, which constrains the statistical power and the generalizability of our findings. Validation in larger patient cohorts and larger animal models is warranted in future studies. Second, although the 5/6 nephrectomy rat model is a well-established paRadigm for SHPT research, it captures only a single time-point snapshot of uremia-driven hyperplasia and may not fully recapitulate the slow progressive process observed in SHPT patients. Third, although the role of RAD51 in SHPT was functionally validated here, the upstream regulators driving its upregulation and its downstream effector mechanisms in parathyroid chief cells await further mechanistic studies, including gene knockdown, overexpression, and rescue experiments.

In conclusion, this study identifies RAD51 as a core hub gene and demonstrates its potential as a biomarker for distinguishing nodular from

diffuse parathyroid hyperplasia in SHPT. Both bioinformatics analyses and in vivo experimental validation consistently show that RAD51 is significantly upregulated in SHPT and sustains aberrant parathyroid cell proliferation by enhancing DNA damage repair to maintain genomic stability. In the SHPT rat model, RAD51 inhibition effectively alleviated disease progression, as evidenced by dose-dependent reductions in serum PTH, improvement of serum calcium levels, attenuation of parathyroid hyperplasia, and suppression of cellular proliferation. Mechanistically, disruption of RAD51-mediated DNA repair leads to accumulation of DNA double-strand breaks and induces caspase-3-mediated apoptosis in parathyroid cells. This study establishes RAD51 as a novel therapeutic target for SHPT, and its mechanism - acting through intracellular DNA repair machinery rather than calcium-sensing receptor signaling - may be particularly relevant to nodular hyperplasia, in which CaSR expression is progressively lost and calcimimetic efficacy is limited. Targeting RAD51 to restore apoptotic sensitivity may offer a targeted therapeutic strategy to curb parathyroid clonal expansion and potentially reduce the need for parathyroidectomy in patients with advanced SHPT.

Acknowledgements

This work was supported by the Scientific Research Fund Project of Yunnan Provincial Department of Education (No. 2025J0274 and No. 2024J0295), the Kunming Health Science and Technology Talent Cultivation Project (No. 2023-SW-Reserve-62), the Kunming Health Science and Technology Talent Cultivation Project - Construction Project of Medical Technology Center (No. 2025-SW-Technology-29), and the Health Science and Technology Research Project of Kunming Municipal Health Commission (No. 2025-09-02-023 and No. 2025-09-02-024).

Disclosure of conflict of interest

None.

Address correspondence to: Yongfeng Li and Wandong Yang, Department of Ultrasound, The First People's Hospital of Kunming, No. 1228, Beijing Road, Panlong District, Kunming 650051, Yunnan, China. E-mail: liyongfeng0307@163.com (YFL); yangwandong1991@163.com (WDY)

References

[1] Wang Y, Liu J, Fang Y, Zhou S, Liu X and Li Z. Estimating the global prevalence of secondary hyperparathyroidism in patients with chronic kidney disease. Front Endocrinol (Lausanne) 2024; 15: 1400891.

[2] Xu Y, Evans M, Soro M, Barany P and Carrero JJ. Secondary hyperparathyroidism and adverse health outcomes in adults with chronic kidney disease. Clin Kidney J 2021; 14: 2213-2220.

[3] Mazzaferro S and Pasquali M. Direct bone effects of calcimimetics in chronic kidney disease? Kidney Int 2019; 95: 1012-1014.

[4] Xu J, Yang Y, Ma L, Fu P and Peng H. Cinacalcet plus vitamin D versus vitamin D alone for the treatment of secondary hyperparathyroidism in patients undergoing dialysis: a meta-analysis of randomized controlled trials. Int Urol Nephrol 2019; 51: 2027-2036.

[5] Block GA, Chertow GM, Sullivan JT, Deng H, Mather O, Tomlin H and Serenko M. An integrated analysis of safety and tolerability of etelcalcetide in patients receiving hemodialysis with secondary hyperparathyroidism. PLoS One 2019; 14: e0213774.

[6] Cocchiara G, Fazzotta S, Palumbo VD, Damiano G, Cajozzo M, Maione C, Buscemi S, Spinelli G, Ficarella S, Maffongelli A, Caternicchia F, Ignazio Lo Monte A and Buscemi G. The medical and surgical treatment in secondary and tertiary hyperparathyroidism. Review. Clin Ter 2017; 168: e158-e167.

[7] Lorenz K, Bartsch DK, Sancho JJ, Guigard S and Triponez F. Surgical management of secondary hyperparathyroidism in chronic kidney disease--a consensus report of the European Society of Endocrine Surgeons. Langenbecks Arch Surg 2015; 400: 907-927.

[8] Ge Y, Yang G, Wang N, Zha X, Yu X, Mao H, Sun B, Zeng M, Zhang B and Xing C. Bone metabolism markers and hungry bone syndrome after parathyroidectomy in dialysis patients with secondary hyperparathyroidism. Int Urol Nephrol 2019; 51: 1443-1449.

[9] Han Y and Wang C. Prediction model of recurrence after parathyroidectomy in secondary hyperparathyroidism. Lin Chuang Er Bi Yan Hou Tou Jing Wai Ke Za Zhi 2023; 37: 282-287.

[10] Tentori F, Wang M, Bieber BA, Karaboyas A, Li Y, Jacobson SH, Andreucci VE, Fukagawa M, Frimat L, Mendelssohn DC, Port FK, Pisoni RL and Robinson BM. Recent changes in therapeutic approaches and association with outcomes among patients with secondary hyperparathyroidism on chronic hemodialysis: the DOPPS study. Clin J Am Soc Nephrol 2015; 10: 98-109.

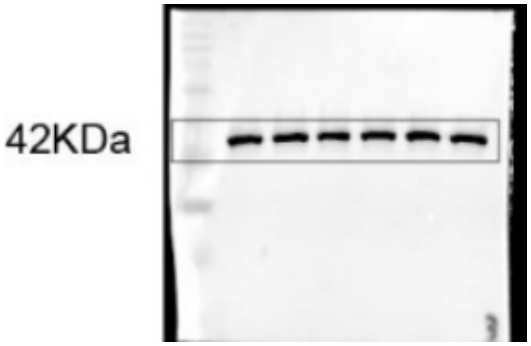
[11] Rodríguez M and Rodríguez-Ortiz ME. Advances in pharmacotherapy for secondary hyperparathyroidism. Expert Opin Pharmacother 2015; 16: 1703-1716.
[12] Hassan A, Khalaily N, Kilav-Levin R, Nechama M, Volovelsky O, Silver J and Naveh-Many T. Molecular mechanisms of parathyroid disorders in chronic kidney disease. Metabolites 2022; 12: 111.
[13] Ilyicheva EA, Shurygina IA, Dremina NN, Bersenev GA and Grigoryev EG. The role of calcium sensitive and vitamin D receptors in the pathogenesis of spoRadic multiple parathyroid gland disease. Probl Endokrinol (Mosk) 2023; 69: 24-34.
[14] Vulpio C, Bossola M, Di Stasio E, Tazza L, Silvestri P and Fadda G. Histology and immunohistochemistry of the parathyroid glands in renal secondary hyperparathyroidism refractory to vitamin D or cinacalcet therapy. Eur J Endocrinol 2013; 168: 811-819.
[15] Shen A, Shi J, Wang Y, Zhang Q and Chen J. Identification of key biomarkers based on the proliferation of secondary hyperparathyroidism by bioinformatics analysis and machine learning. PeerJ 2023; 11: e15633.
[16] Týcová I, Sulková SD, Štěpánková J, Krejčík Z, Merkerová MD, Stránecký V, Hrubá P, Girmanová E, Černoch M, Lipár K, Marada T, Povýšil C and Viklický O. Molecular patterns of diffuse and nodular parathyroid hyperplasia in long-term hemodialysis. Am J Physiol Endocrinol Metab 2016; 311: E720-E729.
[17] Qiu M, Xie Y, Tu L, Zhao M, Yang M, Fang L and Gu J. Overexpressed RAD51 promoted osteogenic differentiation by activating IGF1R/PI3K/AKT pathway in osteoblasts. Acta Biochim Pol 2023; 70: 31-36.
[18] Schürmann L, Schumacher L, Roquette K, Brozovic A and Fritz G. Inhibition of the DSB repair protein RAD51 potentiates the cytotoxic efficacy of doxorubicin via promoting apoptosis-related death pathways. Cancer Lett 2021; 520: 361-373.
[19] Bright SJ, Flint DB, Martinus DKJ, Turner BX, Manandhar M, Ben Kacem M, McFadden CH, Yap TA, Shaitelman SF and Sawakuchi GO. Targeted inhibition of DNA-PKcs, ATM, ATR, PARP, and Rad51 modulate response to X rays and protons. Radiat Res 2022; 198: 336-346.
[20] Shvil Y, Naveh-Many T, Barach P and Silver J. Regulation of parathyroid cell gene expression in experimental uremia. J Am Soc Nephrol 1990; 1: 99-104.
[21] Zhang Q, Qiu J, Li H, Lu Y, Wang X, Yang J, Wang S, Zhang L, Gu Y, Hao CM and Chen J. Cyclooxygenase 2 promotes parathyroid hyperplasia in ESRD. J Am Soc Nephrol 2011; 22: 664-672.
[22] Gene Ontology Consortium, Aleksander SA, Balhoff J, Carbon S, Cherry JM, Drabkin HJ, Ebert D, Feuermann M, Gaudet P, Harris NL, Hill DP, Lee R, Mi H, Moxon S, Mungall CJ, Muruganugan A, Mushayahama T, Sternberg PW, Thomas PD, Van Auken K, Ramsey J, Siegele DA, Chisholm RL, Fey P, Aspromonte MC, Nugnes MV, Quaglia F, Tosatto S, Giglio M, Nadendla S, Antonazzo G, Attrill H, Dos Santos G, Marygold S, Strelets V, Tabone CJ, Thurmond J, Zhou P, Ahmed SH, Asanitthong P, Luna Buitrago D, Erdol MN, Gage MC, Ali Kadhum M, Li KYC, Long M, Michalak A, Pesala A, Pritazahra A, Saverimuttu SCC, Su R, Thurlow KE, Lovering RC, Logie C, Oliferenko S, Blake J, Christie K, Corbani L, Dolan ME, Drabkin HJ, Hill DP, Ni L, Sitnikov D, Smith C, Cuzick A, Seager J, Cooper L, Elser J, Jaiswal P, Gupta P, Jaiswal P, Naithani S, Lera-Ramirez M, Rutherford K, Wood V, De Pons JL, Dwinell MR, Hayman GT, Kaldunski ML, Kwitek AE, Laulederkind SJF, Tutaj MA, Vedi M, Wang SJ, D'Eustachio P, Aimo L, Axelsen K, Bridge A, Hyka-Nouspikel N, Morgat A, Aleksander SA, Cherry JM, Engel SR, Karra K, Miyasato SR, Nash RS, Skrzypek MS, Weng S, Wong ED, Bakker E, Berardini TZ, Reiser L, Auchincloss A, Axelsen K, Argoud-Puy G, Blatter MC, Boutet E, Breuza L, Bridge A, Casals-Casas C, Coudert E, Estreicher A, Livia Famiglietti M, Feuermann M, Gos A, Gruaz-Gumowski N, Hulo C, Hyka-Nouspikel N, Jungo F, Le Mercier P, Lieberherr D, Masson P, Morgat A, Pedruzzi I, Pourcel L, Poux S, Rivoire C, Sundaram S, Bateman A, Bowler-Barnett E, Bye-A-Jee H, Denny P, Ignatchenko A, Ishtiaq R, Lock A, Lussi Y, Magrane M, Martin MJ, Orchard S, Raposo P, Speretta E, Tyagi N, Warner K, Zaru R, Diehl AD, Lee R, Chan J, Diamantakis S, Raciti D, Zarowiecki M, Fisher M, James-Zorn C, PonferRada V, Zorn A, Ramachandran S, Ruzicka L and Westerfield M. The gene ontology knowledgebase in 2023. Genetics 2023; 224: iyad031.
[23] Ogata H, Goto S, Sato K, Fujibuchi W, Bono H and Kanehisa M. KEGG: Kyoto encyclopedia of genes and genomes. Nucleic Acids Res 1999; 27: 29-34.
[24] Wu T, Hu E, Xu S, Chen M, Guo P, Dai Z, Feng T, Zhou L, Tang W, Zhan L, Fu X, Liu S, Bo X and Yu G. clusterProfiler 4.0: a universal enrichment tool for interpreting omics data. Innovation (Camb) 2021; 2: 100141.
[25] Ruifrok AC and Johnston DA. Quantification of histochemical staining by color deconvolution. Anal Quant Cytol Histol 2001; 23: 291-299.
[26] Livak KJ and Schmittgen TD. Analysis of relative gene expression data using real-time quantitative PCR and the 2(-Delta Delta C(T)) method. Methods 2001; 25: 402-408.

[27] Conigrave AD. The calcium-sensing receptor and the parathyroid: past, present, future. Front Physiol 2016; 7: 563.
[28] Lee SM and Pike JW. The vitamin D receptor functions as a transcription regulator in the absence of 1,25-dihydroxyvitamin D(3). J Steroid Biochem Mol Biol 2016; 164: 265-270.
[29] Komaba H and Fukagawa M. FGF23-parathyroid interaction: implications in chronic kidney disease. Kidney Int 2010; 77: 292-298.
[30] Silver J and Naveh-Many T. FGF-23 and secondary hyperparathyroidism in chronic kidney disease. Nat Rev Nephrol 2013; 9: 641-649.
[31] Centeno PP, Herberger A, Mun HC, Tu C, Nemeth EF, Chang W, Conigrave AD and Ward DT. Phosphate acts directly on the calcium-sensing receptor to stimulate parathyroid hormone secretion. Nat Commun 2019; 10: 4693.
[32] Naveh-Many T and Volovelsky O. Parathyroid cell proliferation in secondary hyperparathyroidism of chronic kidney disease. Int J Mol Sci 2020; 21: 4332.
[33] Lu CL, Hou YC, Wu CC, Fang TC, Zheng CM and Lu KC. Combination therapy with nutritional vitamin D and calcimimetics in secondary hyperparathyroidism: a mechanism-based approach to restoring PTH regulation. Front Nutr 2026; 13: 1871009.
[34] Lu CL, Yeih DF, Hou YC, Jow GM, Li ZY, Liu WC, Zheng CM, Lin YF, Shyu JF, Chen R, Huang CY and Lu KC. The emerging role of nutritional vitamin D in secondary hyperparathyroidism in CKD. Nutrients 2018; 10: 1890.
[35] Dantzer C, Dif L, Vaché J, Basbous S, Billottet C and Moreau V. Specific features of ß-catenin-mutated hepatocellular carcinomas. Br J Cancer 2024; 131: 1871-1880.
[36] Marini F, Giusti F, Palmini G, Perigli G, Santoro R and Brandi ML. Genetics and epigenetics of parathyroid carcinoma. Front Endocrinol (Lausanne) 2022; 13: 834362.
[37] Björklund P, Lindberg D, Akerström G and Westin G. Stabilizing mutation of CTNNB1/beta-catenin and protein accumulation analyzed in a large series of parathyroid tumors of Swedish patients. Mol Cancer 2008; 7: 53.
[38] Hao M, Luque-Fernandez MA, Lopez D, Cote K, Newfield J, Connors M and Vaidya A. Benign adrenocortical tumors and the detection of nonadrenal neoplasia. Int J Endocrinol 2019; 2019: 9035407.
[39] Verdelli C, Morotti A, Tavanti GS, Silipigni R, Guerneri S, Ferrero S, Vicentini L, Vaira V and Corbetta S. The core stem genes SOX2, POU5F1/OCT4, and NANOG are expressed in human parathyroid tumors and modulated by MEN1, YAP1, and β-catenin pathways activation. Biomedicines 2021; 9: 637.
[40] Arif M, Vedamurthy BM, Choudhari R, Ostwal YB, Mantelingu K, Kodaganur GS and Kundu TK. Nitric oxide-mediated histone hyperacetylation in oral cancer: target for a water-soluble HAT inhibitor, CTK7A. Chem Biol 2010; 17: 903-913.
[41] Findeisen HM, Gizard F, Zhao Y, Qing H, Heywood EB, Jones KL, Cohn D and Bruemmer D. Epigenetic regulation of vascular smooth muscle cell proliferation and neointima formation by histone deacetylase inhibition. Arterioscler Thromb Vasc Biol 2011; 31: 851-860.
[42] Cobo G, Lindholm B and Stenvinkel P. Chronic inflammation in end-stage renal disease and dialysis. Nephrol Dial Transplant 2018; 33 Suppl 3: iii35-iii40.
[43] Clinical practice guidelines for nutrition in chronic renal failure. K/DOQI, national kidney foundation. Am J Kidney Dis 2000; 35 Suppl 2: S17-S104.
[44] Santamaría I, Alvarez-Hernández D, Jofré R, Polo JR, Menárguez J and Cannata-Andía JB. Progression of secondary hyperparathyroidism involves deregulation of genes related to DNA and RNA stability. Kidney Int 2005; 67: 2267-2279.
[45] Bhattacharya S, Srinivasan K, Abdisalaam S, Su F, Raj P, Dozmorov I, Mishra R, Wakeland EK, Ghose S, Mukherjee S and Asaithamby A. RAD51 interconnects between DNA replication, DNA repair and immunity. Nucleic Acids Res 2017; 45: 4590-4605.
[46] Lopez BS. RAD51-mediated homologous recombination is a pro-tumour driver pathway. Oncogene 2025; 44: 4006-4016.
[47] Guh CL, Lei KH, Chen YA, Jiang YZ, Chang HY, Liaw H, Li HW, Yen HY and Chi P. RAD51 paralogs synergize with RAD51 to protect reversed forks from cellular nucleases. Nucleic Acids Res 2023; 51: 11717-11731.
[48] Bhat KP, Krishnamoorthy A, Dungrawala H, Garcin EB, Modesti M and Cortez D. RADX modulates RAD51 activity to control replication fork protection. Cell Rep 2018; 24: 538-545.
[49] Feu S, Unzueta F, Ercilla A, Pérez-Venteo A, Jaumot M and Agell N. RAD51 is a druggable target that sustains replication fork progression upon DNA replication stress. PLoS One 2022; 17: e0266645.
[50] Arnold A, Brown MF, Ureña P, Gaz RD, Sarfati E and Drüeke TB. Monoclonality of parathyroid tumors in chronic renal failure and in primary parathyroid hyperplasia. J Clin Invest 1995; 95: 2047-2053.
[51] Tominaga Y, Kohara S, Namii Y, Nagasaka T, Haba T, Uchida K, Numano M, Tanaka Y and Takagi H. Clonal analysis of nodular parathyroid hyperplasia in renal hyperparathyroidism. World J Surg 1996; 20: 744-750.

[52] Zhu J, Zhou L, Wu G, Konig H, Lin X, Li G, Qiu XL, Chen CF, Hu CM, Goldblatt E, Bhatia R, Chamberlin AR, Chen PL and Lee WH. A novel small molecule RAD51 inactivator overcomes imatinib-resistance in chronic myeloid leukaemia. EMBO Mol Med 2013; 5: 353-365.

[53] Pan M, Sha Y, Qiu J, Chen Y, Liu L, Luo M, Huang A and Xia J. RAD51 inhibition shows antitumor activity in hepatocellular carcinoma. Int J Mol Sci 2023; 24: 7905.

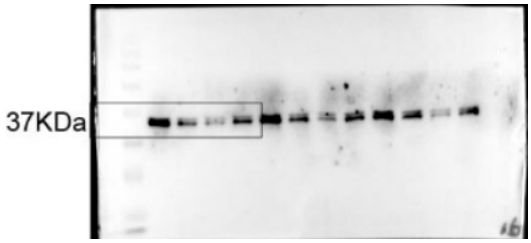
[54] Mendoza FJ, Lopez I, Canalejo R, Almaden Y, Martin D, Aguilera-Tejero E and Rodriguez M. Direct upregulation of parathyroid calcium-sensing receptor and vitamin D receptor by calcimimetics in uremic rats. Am J Physiol Renal Physiol 2009; 296: F605-613.



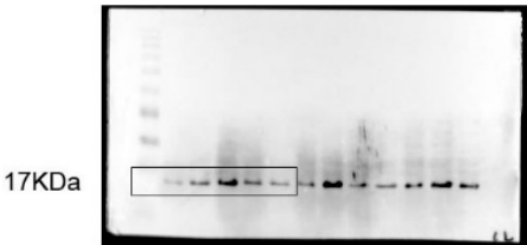
Supplementary Figure 1. Full uncropped images of the β-actin western blots shown in **Figure 8A**.



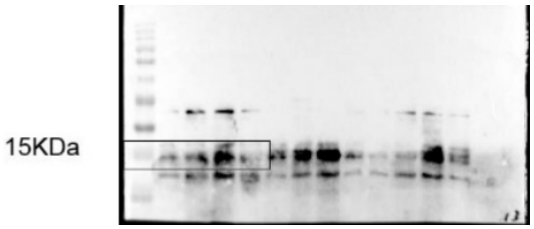
Supplementary Figure 2. Full uncropped images of the RAD51 western blots shown in **Figure 8A**.



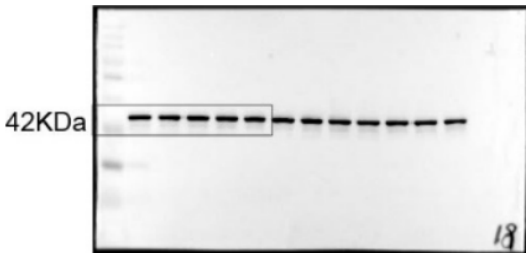
Supplementary Figure 3. Full uncropped images of the RAD51 western blots shown in **Figure 10B**.



Supplementary Figure 4. Full uncropped images of the cleaved-caspase-3 western blots shown in **Figure 10B**.



Supplementary Figure 5. Full uncropped images of the γH2AX western blots shown in **Figure 10B**.



Supplementary Figure 6. Full uncropped images of the β-actin western blots shown in **Figure 10B**.